Destructive Potential of Planetary Meteotsunami Waves beyond the Hunga Tonga–Hunga Ha'apai Volcano Eruption

Cléa Denamiel, Sergiy Vasylkevych, Nedjeljka Žagar, Petra Zemunik, and Ivica Vilibić

ABSTRACT: Worldwide tsunamis driven by atmospheric waves—or planetary meteotsunami waves—are extremely rare events. They mostly occur during supervolcano explosions or asteroid impacts capable to generate atmospheric acoustic-gravity waves including the Lamb waves that can circle the globe multiple times. Recently, such ocean waves have been globally recorded after the Hunga Tonga–Hunga Ha'apai volcano eruption on 15 January 2022, but did not pose any serious danger to the coastal communities. However, this study highlights that the mostly ignored destructive potential of planetary meteotsunami waves can be compared to the well-studied tsunami hazards. In practice, several process-oriented numerical experiments are designed to force a global ocean model with the realistic atmospheric response to the Hunga Tonga–Hunga Ha'apai event rescaled in speed and amplitude. These simulations demonstrate that the meteotsunami surges can be higher than 1 m (and up to 10 m) along more than 7% of the world coastlines. Planetary meteotsunami waves thus have the potential to cause serious coastal damages and even human casualties during volcanic explosions or asteroid impacts either releasing intense acoustic energy or producing internal atmospheric gravity waves triggering the deep-ocean Proudman resonance at a speed of ~212 m s^{-1}. Based on records of catastrophic events in Earth's history, both scenarios are found to be realistic, and consequently, the global meteotsunami hazards should now be properly assessed to prepare for the next big volcanic eruption or asteroid impact even occurring inland.

KEYWORDS: Extreme events; Sea level; Surface layer; Numerical analysis/modeling; Ocean models

AFFILIATIONS: **Denamiel and Vilibić**—Division for Marine and Environmental Research, Ruđer Bošković Institute, Zagreb, Croatia; **Vasylkevych and Žagar**—Meteorological Institute, Universität Hamburg, Hamburg, Germany; **Zemunik**—Institute of Oceanography and Fisheries, Split, Croatia

Catastrophic events such as volcano explosions (Choi et al. 2003) or asteroid impacts (Chapman and Morrison 1994; Morgan et al. 2022) are known to cause extreme damage near their epicenters but also to affect the entire planet through megatsunamis (Kharif and Pelinovsky 2005), acidification of the atmosphere and ocean (Ohno et al. 2014), aerosol-driven reduction of solar radiation (Kring et al. 1996), and many other planetary-scale processes. However, the global impact of atmospheric waves (Matoza et al. 2022) generated during these events, including acoustic-gravity waves (Yeh and Liu 1974) and the most prominent Lamb waves (Lamb 1911; Bretherton 1969), remains sporadically documented. Lamb waves propagate horizontally in the atmosphere with a speed close to the mean sound speed (Dragoni and Santoro 2020) and can circle the globe multiple times (Press and Harkrider 1966; Amores et al. 2022). They are associated with surface pressure oscillations of several hectopascals (hPa) per minute (Press and Harkrider 1966; Harrison 2022) and their energy is dissipated toward the thermosphere (Forbes et al. 1999) via the ionosphere. In the worldwide oceans, they excite atmospheric tsunamis or meteotsunamis—long waves in the tsunami frequency band generated by atmospheric disturbances (Pattiaratchi and Wijeratne 2015; Rabinovich 2020)—which spread with much greater speeds than tsunami waves generated by volcanic eruptions or seismic activity (Satake et al. 2020; Adam 2022).

The existence of planetary-scale Lamb wave–driven meteotsunamis has been first hypothesized after the catastrophic eruption of the Krakatau volcano in 1883 (Press and Harkrider 1966; Self and Rampino 1981). The then sparse and low-quality tide gauge global network recorded (i) a mismatch between the analytically derived and observed arrival times of the tsunami waves resulting from the volcano collapse in the Pacific Ocean, and (ii) worldwide sea level oscillations as far away from the source as the English Channel. Nowadays, meteotsunamis locally generated by weather systems are known to be fully amplified when an atmospheric disturbance travels at a speed U similar to the ocean waves ($c = \sqrt{gH}$, with g the gravity and H the ocean depth)—i.e., when the Froude number (Fr = U/c) is close to 1.0 (Vilibić 2008). Under this condition, also referred as Proudman resonance (Proudman 1929), the energy of the atmospheric disturbance is efficiently transferred to the background ocean waves which are amplified by an order of magnitude compared to the inverse barometer effect (Vilibić 2008). In terms of coastal risks, the meteotsunami surges (i.e., the maximum coastal sea levels) can be on the order of several meters as observed in the Adriatic Sea in 1978 (Pattiaratchi and Wijeratne 2015; Rabinovich 2020). They can thus cause extensive infrastructure damage, navigation and beach safety concerns, and human casualties (Pattiaratchi and Wijeratne 2015; Rabinovich 2020). However, the socioeconomic impact of meteotsunamis generated by weather systems is generally geographically limited to specific bays and littoral areas (at most a hundred kilometers of coastline).

The recent explosive eruption of the Hunga Tonga–Hunga Ha'apai volcano (Hunga eruption hereafter) on 15 January 2022 was exceptionally well observed by satellites and recorded worldwide by thousands of microbarographs, seismometers, and tide gauges (Matoza et al. 2022; Amores et al. 2022; Harrison 2022; Adam 2022; Wright et al. 2022). This rare event

thus provided a unique opportunity for the scientific community to revisit the global impact of meteotsunamis. Consequently, in this study, we assess the destructive potential of the planetary meteotsunami waves, beyond the Hunga eruption, with state-of-the-art atmospheric and oceanic global models. First, we simulate the main wave signals of the Hunga event to describe the baseline atmosphere–ocean dynamics generated by the volcanic eruption. Then, with process-oriented simulations, we derive the conditions most favorable to extreme worldwide meteotsunami surges. Finally, we investigate the aptitude of catastrophic events to generate extreme meteotsunami surges similar to those obtained with the process-oriented simulations.

Material and methods

Numerical experiments. A total of 12 different simulations are analyzed in this study. First, the Baseline simulation is reproducing as realistically as possible the Lamb waves in the atmosphere and the meteotsunamis in the ocean for a 5-day-long period after the Hunga eruption. Then, ten 2-day-long process-oriented simulations are performed in order to find the speeds of the atmospheric waves leading to the maximum meteotsunami amplification under full Proudman resonance. For these simulations, the timeline of the Baseline atmospheric response is artificially rescaled by 1.25, 1.40, 1.50, 1.60, 1.65, 1.75, 2.00, 3.00, 4.00, and 5.00, thereby proportionally reducing the speed of the Lamb waves. The simulation leading to full Proudman resonance is referred to as simulation P. Finally, in the last 2-day-long simulation (simulation A) used to assess the destructive potential of truly catastrophic events, the amplitude of the Lamb waves used in the Baseline simulation is multiplied by 10 before forcing the ocean model.

Atmospheric response in Transient Inertia–Gravity And Rossby wave dynamics model. A Lamb wave is an acoustic-gravity wave mode often considered in the isothermal atmosphere at rest. The nondispersive Lamb waves propagate horizontally with a phase velocity weakly depending on the vertical background temperature profile. For a standard atmosphere, this speed is $U \approx 312$ m s^{-1} (Harrison 2022; Press and Harkrider 1962). In the barotropic framework (Kasahara 1977), a horizontally propagating surface gravity wave has a phase speed $c = \sqrt{gD}$, where D is the mean fluid depth. This approach extends into the baroclinic atmosphere, where D becomes the equivalent depth, or the eigenvalue of the vertical structure equation for the linearized primitive equations (Cohn and Dee 1989), associated with a single vertical mode, an eigenvector of the vertical structure equation. Cohn and Dee (1989) showed that the global, bounded atmosphere has the equivalent depth $D \approx 10$ km, with associated gravity wave speed $c \approx 313$ m s^{-1}. This matches the speed of the main wave triggered by volcanic eruptions.

The above observation supports the use of the barotropic version of the Transient Inertia–Gravity And Rossby wave dynamics (TIGAR) model (Vasylkevych and Žagar 2021) for the Lamb wave simulation after the Hunga eruption. The TIGAR model solves the primitive equations in terrain-following coordinates using the Hough harmonics as the basis functions. In this representation, the Rossby and inertia–gravity waves are prognostic quantities, an approach especially suitable for studying gravity wave dynamics on the sphere. The model includes a realistic orography on the computational grid T170 that corresponds to the regular Gaussian grid of 680 and 320 grid points in the longitudinal and latitudinal directions, respectively. Presence of orography ensures the deflection of the Lamb wave by major mountain ranges (Movie S1 in the online supplementary material). The exponential fourth-order Runge–Kutta scheme (Cox and Matthews 2002) with a 3-min time step was used for time integration. The dissipative processes were represented through the linear damping term in the continuity equation with damping scale defined by a tuning parameter τ.

The Hunga eruption was modeled by specifying an initial condition in the form of large amplitude Gaussian geopotential height perturbation centered on the volcano location, superimposed on the barotropic atmosphere at rest. Noting that in the barotropic model the geopotential height and pressure perturbations are proportional, the amplitude of the pressure perturbation at the source Δp = 35.1 hPa and the scale parameter σ = 2.7° were optimized to match the observed wavelength of the wave response, while dissipation time scale τ = 3.4 days was obtained by best fit of the wave amplitude to the observed pressure fluctuations at the evaluation sites. The TIGAR global simulations of the observed Lamb wave generated by the Hunga eruption has been previously evaluated by Themens et al. (2022).

ATAL ocean model. The Atmospheric Tsunamis Associated with Lamb waves (ATAL) model was specifically developed and implemented to reproduce the planetary meteotsunami waves generated by intense atmospheric forcing. It is based on the barotropic version (2DDI) of the Advanced Circulation (ADCIRC) unstructured model (Luettich et al. 1991) which solves the shallow-water equations in the ocean. Recently, the ADCIRC model has been updated for global applications (Pringle et al. 2021) and extensively used to study and forecast meteotsunami events (Denamiel et al. 2019, 2020, 2022) at the regional and nearshore scales.

The ATAL unstructured mesh used in this study was designed not only to properly capture the atmosphere–ocean interactions at the basin scale, but also to partially reproduce the coastal and nearshore meteotsunami transformation. It was produced with the OceanMesh2D (Roberts et al. 2019) software for resolutions ranging from 20 km in the deep ocean to 1.5 km along the worldwide coastlines using (i) the Global Self-consistent, Hierarchical, High-resolution Geography Database (GSHHG) fine resolution coastline (Wessel and Smith 1996) and (ii) the bathymetry from the GEBCO_2021 15-arc-s grid (Weatherall et al. 2021). The final mesh is composed of 6,864,084 nodes forming 13,306,437 triangular elements with a bathymetry ranging from a minimum of 1 m at the coast to 9,823 m in the deepest part of the ocean.

In terms of numerical setup, the ATAL model uses the optimal configuration of the ADCIRC model for global simulations (Luettich et al. 1991) with a time step of 1 s, a spatially varying Manning friction coefficient (Holland 1998), no tidal forcing, no wind forcing, and a 3-min (for the Baseline simulation) pressure forcing adding the Lamb wave oscillations from the TIGAR model to the 1,013 hPa uniform background pressure. In its actual configuration, the ATAL model runs on 400 CPUs (i.e., subdomains) and produces 1 day of simulation in 2 h of computation on the European Centre for Medium-Range Weather Forecasts (ECMWF) High-Performance Computing (HPC) facilities.

Observations and ATAL model evaluation. The ATAL model evaluation is performed, for the sea levels only, over a period of 5 days after the Hunga eruption. First, the 1-min sea level data at 86 worldwide tide gauge stations are extracted from the Intergovernmental Oceanographic Commission Sea Level Station Monitoring Facility (VLIZ 2022). At each of the 86 stations, the high-frequency signal (i.e., mostly the tsunami and meteotsunami waves and the local processes such as harbor resonance) is obtained by using a 2-h Kaiser–Bessel filter on the quality-checked observational data. Second, the 3-min sea level outputs of the Baseline simulation are extracted at the closest mesh node from the 86 station locations and the 1-min measurements are resampled to 3-min. The evaluation of the sea level heights is thus performed for 86 observation–model pairs of 2,401-point long records including potentially missing data. Third, for the comparison of the times of the maximum, the model and observation maximum sea levels and associated times are extracted for the entire 5-day period at each of the 86 stations. The evaluation is thus only performed for 86 observation–model pairs of "arrival" times. Then, as both tsunami and meteotsunami waves were generated after the eruption and no straightforward method can easily differentiate them in the observations,

the tide gauge stations are separated in two groups: (i) the "tsunami and meteotsunami" group, including 43 stations mostly located in the Pacific Ocean, and (ii) the "meteotsunami only" group, including the 43 remaining locations where no tsunami impact was recorded. Finally, as this process-oriented study focuses more on the general reproduction of the Lamb wave–driven meteotsunami waves at the planetary scale than the precise reproduction of the extreme sea levels and their timing at a precise location, quantile–quantile plots are used for the ATAL model evaluation for the two groups of stations.

Extreme sea level analysis. The outputs of the ATAL model analyzed in this study are (i) the 3-min sea levels for Baseline simulation and simulation A as well as the 4.5-min sea levels for simulation P, only used to produce the animations presented in Movies S1 and S2, and (ii) the maximum sea levels automatically computed at every time step and obtained after 2 days of simulation. The maximum sea levels are analyzed (i) spatially over the entire ATAL domain and (ii) for the ATAL mesh nodes only located along the coastline (referred as meteotsunami surges). The percentages of meteotsunami surge occurrences above 1.00 m are calculated as the ratio between the number of coastal mesh nodes fulfilling the criteria and the total number of coastal mesh nodes multiplied by 100%. The percentages of Froude coverage are calculated as the ratio between the sum of the areas of each mesh element with three mesh nodes fulfilling the criteria and the sum of the areas of all mesh elements multiplied by 100%.

Atmosphere–ocean dynamics generated by the Hunga eruption

We carried out a 5-day-long simulation of the Lamb wave–driven ocean waves generated by the Hunga eruption (Baseline simulation hereafter) by coupling offline ATAL with the atmospheric simulation by TIGAR.

The simulated atmosphere–ocean dynamics is qualitatively described with the animation of the first 48 h of the Baseline simulation (Movie S1 in supplementary material). TIGAR reproduces the atmospheric Lamb waves with amplitudes reaching up to 7 hPa near the source and 0.5–3 hPa worldwide, in a good agreement with the microbarograph observations. The modeled Lamb wave speed is about 318 m s^{-1}, similar to the observed (Wright et al. 2022), and similar to that estimated for the Krakatoa eruption in 1883 (Taylor 1929). Used with realistic topography, TIGAR also emulates some wave deformations observed by satellites (Matoza et al. 2022; Wright et al. 2022) as the Lamb wave travels around the world multiple times. In the ocean, away from the shore, the meteotsunamis simulated by ATAL travel at a speed similar to the Lamb wave and have amplitudes of 1–3 cm in the deep ocean and up to 5 cm near the source. As less than 1% of the ocean depths are greater than 6,000 m, the Froude number is almost always greater than 1.3 and not favorable to Proudman resonance for Lamb wave–driven meteotsunamis.

Consequently, away from the shore, the planetary meteotsunami waves are not amplified by resonance and their amplitudes depend only on the intensity of the atmospheric forcing. However, nearshore wave transformations such as shoaling, reflection, refraction, and diffraction (Titov et al. 2005) are the main drivers of the meteotsunami surges along the coastlines. Additionally, ATAL produces secondary deep-ocean waves with amplitudes larger than the primary meteotsunamis. This sequencing process is well-documented in the tsunami-research community and is caused by the irregular bathymetry of the ocean basins which leads to multipathing as well as focusing/defocusing of the planetary meteotsunami waves (Okal and Synolakis 2016).

Quantitatively, ATAL reproduces very well the distribution of the 3-min coastal sea level observations (meteotsunamis only, Figs. 1a,c) recorded at 43 tide gauge locations not affected by tsunamis due to the volcanic eruption (volcanic tsunamis hereafter). For the 43 other tide
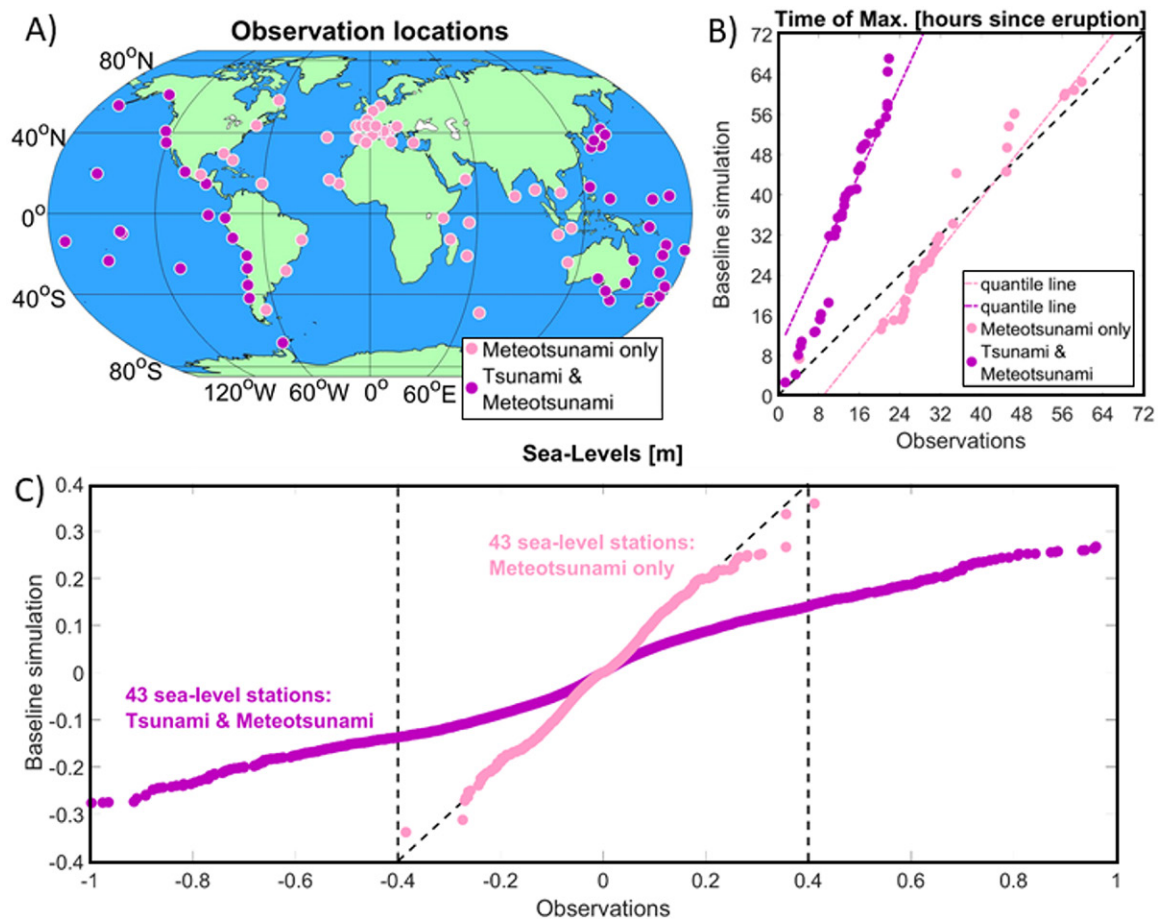
Fig. 1. Validation of the numerical simulation of Lamb wave–driven meteotsunamis generated during 5 days after the Hunga eruption. (a) Worldwide stations, and quantile–quantile plots of observed and simulated (b) time of the meteotsunami surges (time of max) and (c) 3-min sea levels at 43 stations affected by meteotsunamis only and 43 stations affected by both tsunamis and meteotsunamis.

gauge stations located mostly in the Pacific Ocean (tsunami and meteotsunami, Figs. 1a,c), the simulated meteotsunamis are about 2–3 times smaller than the observed volcanic tsunamis. A relatively small mismatch in timing exists between the meteotsunami surges in the Baseline simulation and the observations (Fig. 1b). This is mostly explained by the fact that the nearshore wave transformation is not properly represented by the 1.5 km coastal resolution of the ATAL model. For the tsunami and meteotsunami stations, the observed maximum sea levels agree with the arrival of the volcanic tsunamis in the first 24 h after the eruption, while the simulated meteotsunami surges occur during the first 72 h of simulation. The maximum sea levels during the first 48 h of the Baseline simulation are presented in Fig. 2. Meteotsunamis are higher than 5 cm only near the source of the eruption in the deep ocean, along the coastlines directly hit by the waves (e.g., Japan, east North America) or close to the focal point of the atmospheric Lamb waves in northwestern Africa (Fig. 2a). Deep-ocean amplifications up to 3 cm occur along changing bathymetry, such as the southern Pacific ridges, capable to transfer and channel the wave energy over long distances (Okal and Synolakis 2008). The cumulative density function (CDF; Fig. 2b) shows that meteotsunami surges above 20 cm hit less than 1% of the worldwide coastal areas. Consequently, we find that meteotsunami surges generated by the Hunga eruption could not pose any significant threat to the coastal communities, although strong coastal currents (i.e., rip currents) associated with meteotsunamis of moderate amplitude can be responsible for drowning (Linares et al. 2019).
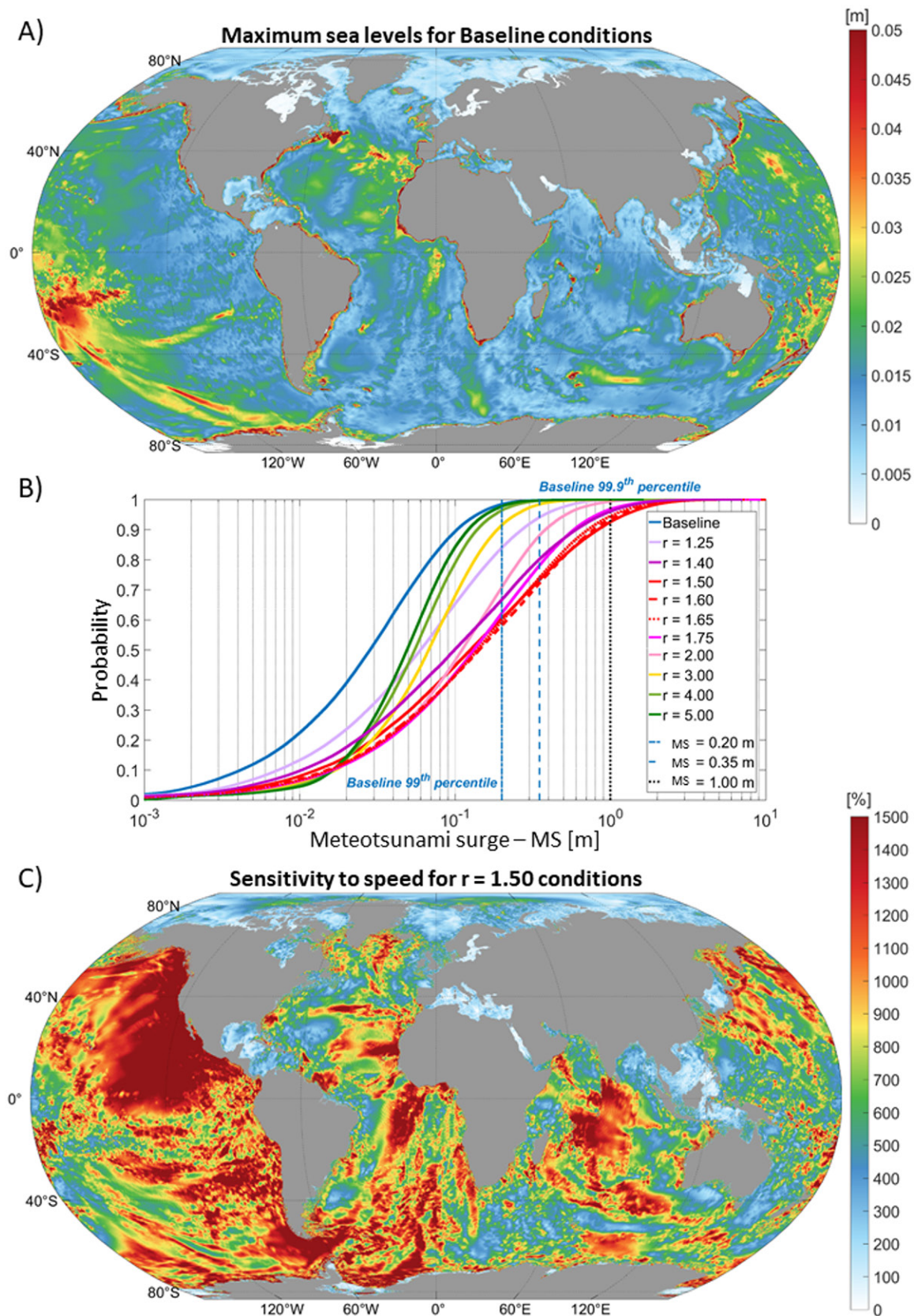
Fig. 2. Distributions of the maximum sea levels after 48 h of simulation. (a) Baseline simulation (*r* = 1.00), (b) cumulative density functions of the meteotsunami surges (MS) for Baseline and sensitivity simulations with scaling factor *r* applied to the atmospheric wave phase speed varying between 1.25 and 5.00, and (c) sea level ratios between the *r* = 1.50 conditions and the Baseline simulation multiplied by 100%. Scaling factor *r* = 1.50 generates the highest meteotsunami surges.

Favorable conditions for destructive meteotsunami surges

Based on the known meteotsunami generation mechanisms (Vilibić 2008), we identified two processes capable of increasing the destructive potential—defined as the maximum surges—produced by the planetary meteotsunami waves during the Hunga event. The first is the deep-ocean Proudman resonance which only depends on the speed of the atmospheric forcing. And the second is the inverse barometer effect which implies that larger meteotsunami waves should be generated by larger Lamb waves.

Deep-ocean Proudman resonance. To determine the necessary atmospheric conditions for deep-ocean Proudman resonance and, hence, the maximal amplification of the planetary meteotsunami waves, we divided the Lamb wave speed, simulated by TIGAR in the Baseline simulation, by a scaling factor r ranging from $r = 1.25$ ($U \approx 254$ m s^{-1}) to $r = 5.00$ ($U \approx 64$ m s^{-1}). We then forced a total of 10 additional ATAL simulations of 48-h length with the obtained atmospheric waves.

Resulting CDF distributions of the meteotsunami surges (Fig. 2b) show that the most extreme meteotsunami surges occur for scaling factors between $r = 1.50$ and 1.65 and, thus, for atmospheric waves with phase speeds between $U \approx 193$ and 212 m s^{-1}. Under these conditions, 30% of the worldwide coastlines are hit by meteotsunami surges higher than 35 cm (the 99.9th-percentile value of the Baseline simulation). More importantly, the highest meteotsunami surges are obtained for $r = 1.50$ ($U \approx 212$ m s^{-1}), which is consequently assumed to be the condition most favorable to Proudman resonance. Additionally, as the ocean depths strongly impact the resonance, the meteotsunami amplification is highly geographically dependent, even under full Proudman resonance ($r = 1.50$; Fig. 2c). It is particularly pronounced west of the northwest American coast where the maximum sea levels are 15 times greater than in the Baseline simulation. Somewhat weaker, but still a significant meteotsunami amplification (i.e., about 80%–90%) is obtained in the shallower oceans and seas (e.g., the Arctic Ocean and the Mediterranean Sea).

For atmospheric phase speeds obtained with $r \leq 1.40$ or $r \geq 1.75$ (i.e., conditions out of Proudman resonance), the occurrences of meteotsunami surges above 1.00 m are small (below 4.5%) and even close to zero for $r = 1.25$ and $r \geq 3.00$ (Fig. 3b). Additionally, for $r \geq 3.00$, the spatial coverage of the resonance favorable conditions is reduced to coastal and shelf regions too narrow to allow for strong coastal amplifications. For the resonance favorable conditions ($r = 1.50$–1.65), 35%–50% of the whole oceans have Froude numbers close to 1.0 (0.9 < Fr < 1.1) while 5.5%–7.5% of the worldwide coastlines are hit by meteotsunami surges larger than 1.00 m (Figs. 3a,b) and up to 10 m at some locations (Fig. 2b). Further, a strong spatial correlation also exists between the maximal meteotsunami amplifications (Fig. 2c) and the resonance favorable conditions for $r = 1.50$–1.65 (Fig. 3a).

Tenfold increase of the Lamb wave amplitude. To derive the destructive potential of events releasing more acoustic energy than the Hunga eruption, an additional ATAL simulation (simulation A) was forced by Lamb waves with 10-times-greater amplitude than in the Baseline simulation. Hereafter, the results of simulation A are compared to the simulation under full Proudman resonance (i.e., $r = 1.50$; simulation P).

Qualitatively, the deep-ocean meteotsunami amplification is similar (up to 20 cm) for both simulations (A and P), but the propagation and coastal amplification processes are visibly different (movie S2 in supplementary material). Simulation P develops meteotsunamis following the passage of the Lamb waves in the deep ocean. These waves are strongly modified in the nearshore and coastal areas, where their reflection leads to large amplitude increase over nearly the entire ocean basins (e.g., along the west coast of North America). In contrast, in simulation A (similarly to the Baseline simulation), the main Lamb wave–driven
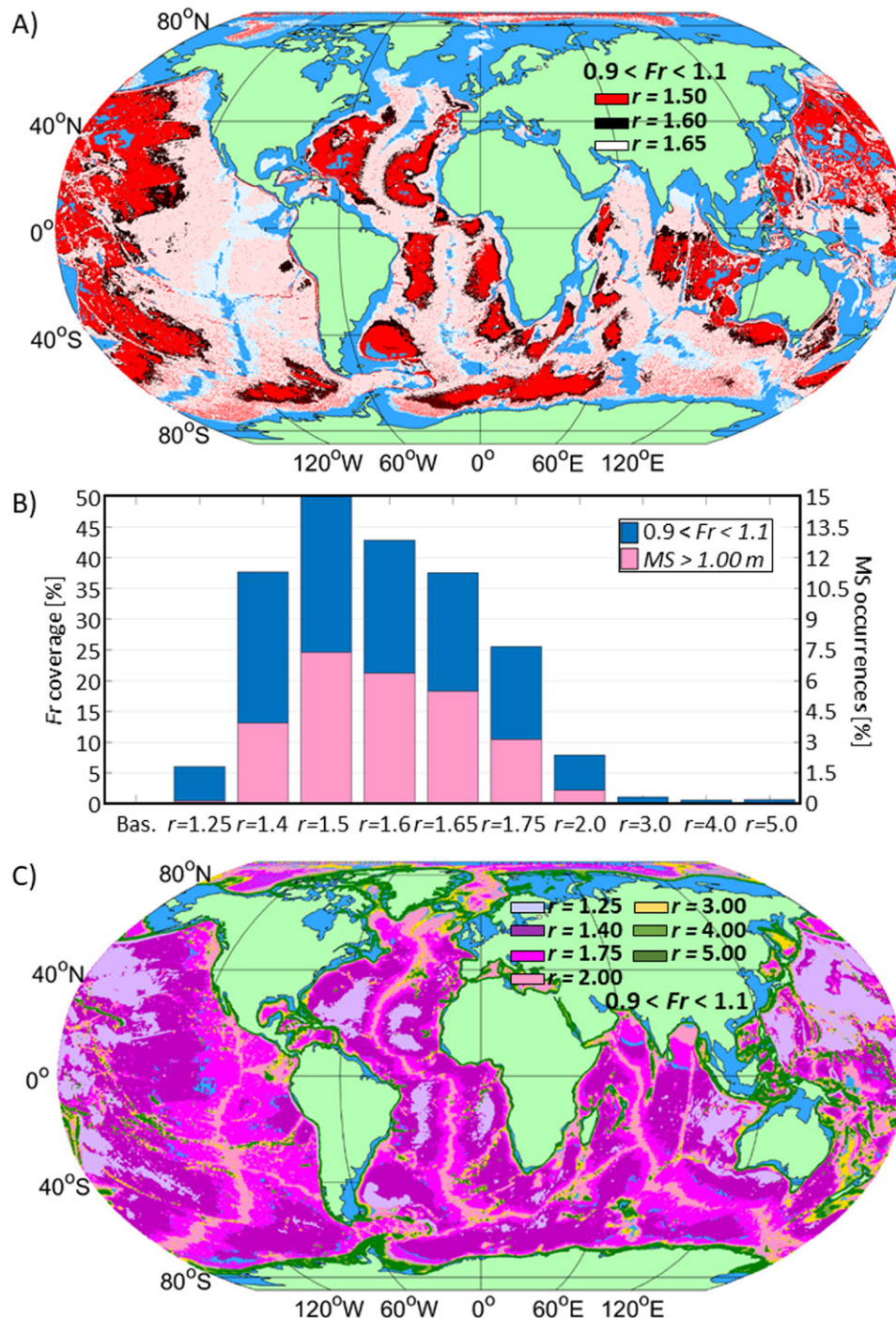
Fig. 3. Distributions of the Froude numbers favorable to Proudman resonance (0.9 < Fr < 1.1). Spatial plots for the (a) highest (r = 1.50, 1.60, 1.65) and (c) lowest (r = 1.25, 1.75, 2.00, 3.00, 4.00, 5.00) resonance conditions and (b) spatial coverage (i.e., area favorable to Proudman resonance vs total area) compared to the occurrences of meteotsunami surges (MS) above 1.00 m.

meteotsunamis are followed by secondary waves of higher amplitudes in all ocean basins and no strong reflection occurs near the coasts where the waves are amplified mostly through shoaling, refraction, and diffraction.

Quantitatively, in the deep ocean, the differences in maximum sea levels (A–P; Fig. 4a) exceed 10 cm in the vicinity of the eruption as well as in the Oceania, the Mediterranean Sea, and the North Atlantic basin. However, at the locations where strong reflection occurs in simulation P, they are below −10 cm (e.g., along the northwest–southwest American coasts). Nonetheless, the CDF distributions and the percentage of coastlines with meteotsunami surges higher than 1.00 m are almost identical for both simulations (Fig. 4b). This shows that, along
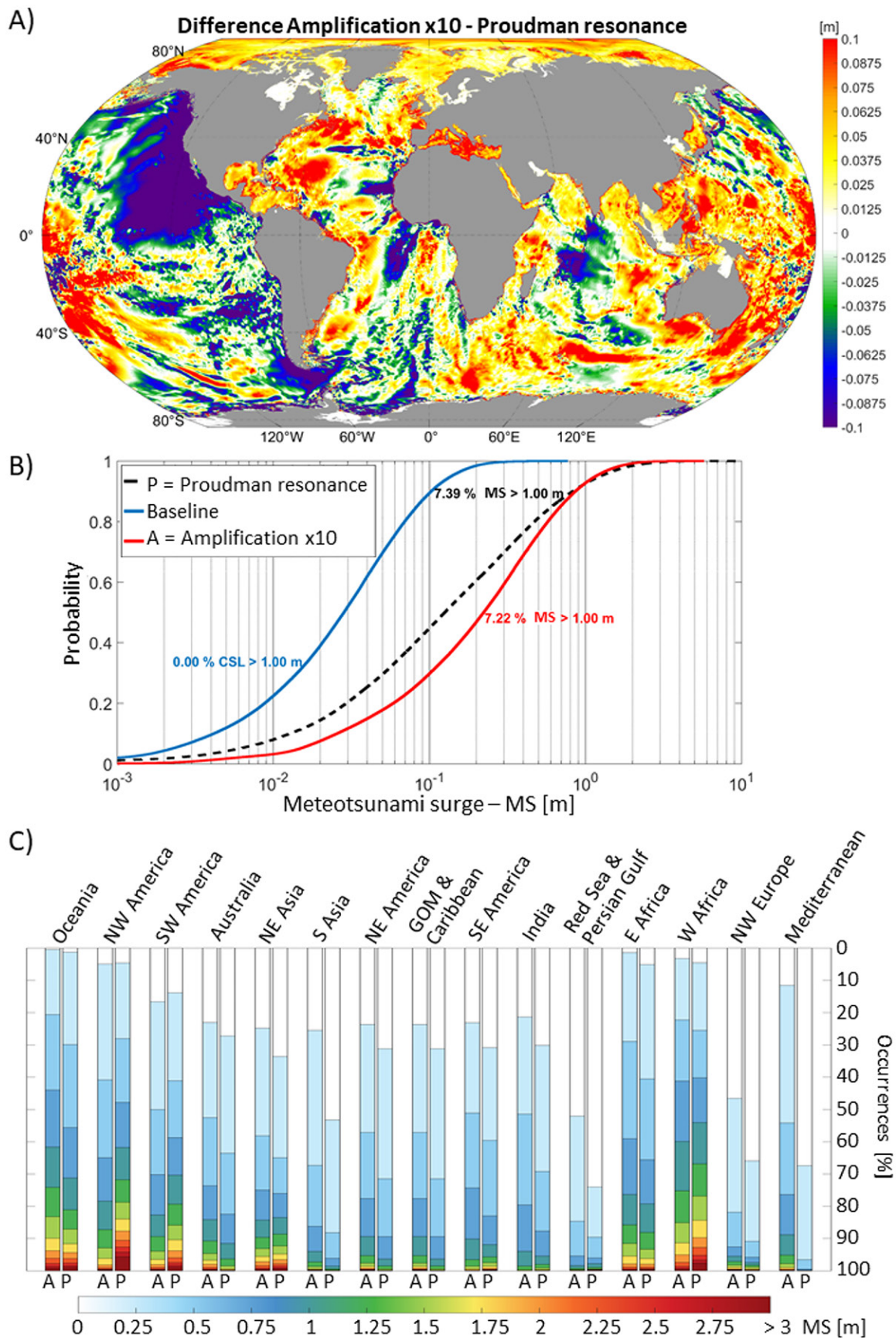
Fig. 4. Maximum sea levels obtained under Proudman resonance conditions (i.e., *r* = 1.50) and tenfold amplification of the Lamb wave amplitudes in the atmosphere. (a) Spatial plot of differences and meteotsunami surges as (b) cumulative density functions and (c) distributions by coastal subdomains.

the coasts, the meteotsunami amplification driven by tenfold-amplified Lamb waves matches the conditions under full Proudman resonance.

Additionally, the distributions of meteotsunami surges along different coastal regions (Fig. 4c) confirm that the strong reflection of the meteotsunamis in simulation P also impacts the coastal hazards. Indeed, the occurrences of extreme values above 1.50 m are 2–5 times higher in simulation P than in simulation A for the northwest and southwest Americas and west African coastal areas. In contrast, simulation A generates 5%–8% of extreme values above 1.50 m in microtidal semienclosed basins (e.g., Mediterranean Sea, Gulf of Mexico) not affected by simulation P. As these low-lying coastal areas are well-populated, the modeled meteotsunami surges could pose a serious danger to the coastal communities.

In terms of destructive potential, we thus find that, under full Proudman resonance or for Lamb waves with 10-times-greater amplitude than the Hunga event, meteotsunami surges can reach similar heights (i.e., more than 1 m and up to 10 m) but are likely to hit more coastal areas (i.e., more than 7% of the worldwide coastlines) than during catastrophic tsunami events.

Implications in terms of global meteotsunami hazards

Realistically, the condition for full Proudman resonance cannot be reached by Lamb waves always traveling at $U \approx 318$ m s^{-1} and volcanic eruptions similar to the Hunga event cannot generate tenfold amplified atmospheric forcing. However, based on records of catastrophic events in Earth's history (Chapman and Morrison 1994; Morgan et al. 2022), we argue that volcanic eruptions, asteroid impacts, and explosions of anthropogenic origin have the potential to generate intense planetary meteotsunami waves associated with destructive surges along the populated coastal areas.

On the one hand, during the first hours after the Hunga explosion, seismoacoustic and satellite observations (Matoza et al. 2022; Wright et al. 2022) suggest the presence of several internal gravity waves likely generated by a complex eruption sequence and traveling with speeds between 240 and 270 m s^{-1}. Even though lower than the Lamb waves, the speed of these internal gravity waves is still not favorable to the Proudman resonance as it corresponds to $r = 1.25$ (Fig. 3). Nonetheless, this speed is thought to be largely controlled by the vertical profile of the temperature perturbation introduced by the eruption. This suggests that under favorable conditions (e.g., a steeper initial temperature anomaly profile above the tropopause), large amplitude waves with speeds favorable to Proudman resonance can be generated.

On the other hand, supervolcanos or asteroid impacts (Chapman and Morrison 1994; Ohno et al. 2014)—with return periods of 100–1,000 years (Mason et al. 2004)—have the potential to generate intense Lamb waves as they release about 10 to 1 billion megatons of energy (i.e., 700 to 70 billion times the energy of the atomic bomb dropped on Hiroshima, Japan, in 1945). For example, the Krakatoa eruption of 1883 released 20–50 times more energy than the Hunga eruption (Lowe and de Lange 2000) and generated stronger meteotsunamis in the Atlantic Ocean (Pelinovsky et al. 2005). It is therefore possible that more intense atmospheric forcing, as simulated in this study, could lead to destructive meteotsunami surges far from the epicenter of the catastrophic event.

Another important consideration is that the generation of planetary meteotsunami waves could even be possible for inland events such as the Tunguska explosion (Chyba et al. 1993). In such circumstances, meteotsunami surges would be the principal hazard along the worldwide coastlines. However, during volcanic explosions or asteroid impacts, early warning systems, mostly designed for tsunamis, are not presently taking into account the hazards posed by meteotsunamis in their modeling suites.

Overall, this exploratory study confirms the necessity to properly investigate the meteotsunami hazards during catastrophic volcanic eruptions and asteroid impacts at sea or inland.

As these events are extremely rare and occur at the geological scale, only the systemic reproduction and forecast of global meteotsunami surges associated with fast atmospheric waves could answer the main questions raised by this study. Can internal gravity waves associated with explosions trigger the deep-ocean Proudman resonance? Can catastrophic events produce Lamb waves 10 times higher than during the Hunga eruption? Can an inland volcano eruption/asteroid impact cause meteotsunami surges comparable to tsunamis? This study thus opens the door to a new field of research that requires a multidisciplinary approach involving geologists, volcanologists, atmospheric scientists, oceanographers, and numerical modelers.

In summary, the destructive potential of the planetary meteotsunami waves remained mostly unexplored before the Hunga eruption. In this study we have demonstrated, for the very first time, that atmospheric planetary waves with phase speeds matching the deep-ocean Proudman resonance criterion or having a large amplitude can produce extreme surges worldwide. Further, contrarily to the near-field tsunamis, destructive meteotsunami surges could cause serious damages to the coastal infrastructure, sink boats in harbors, and take a heavy toll in human lives at numerous locations along the shores far away from the epicenter of a catastrophic event. Consequently, the historically underestimated meteotsunami hazards should be properly assessed and quantified to better prepare for the next big events generating planetary-scale fast atmospheric waves.

References

Adam, D., 2022: Tonga volcano eruption created puzzling ripples in Earth's atmosphere. *Nature*, **601**, 497, https://doi.org/10.1038/d41586-022-00127-1.

Amores, A., S. Monserrat, M. Marcos, D. Argüeso, J. Villalonga, G. Jordà, and D. Gomis, 2022: Numerical simulation of atmospheric Lamb waves generated by the 2022 Hunga-Tonga volcanic eruption. *Geophys. Res. Lett.*, **49**, e2022GL098240, https://doi.org/10.1029/2022GL098240.

Bretherton, F., 1969: Lamb waves in a nearly isothermal atmosphere. *Quart. J. Roy. Meteor. Soc.*, **95**, 754–757, https://doi.org/10.1002/qj.49709540608.

Chapman, C. R., and D. Morrison, 1994: Impacts on the Earth by asteroids and comets: Assessing the hazard. *Nature*, **367**, 33–40, https://doi.org/10.1038/367033a0.

Choi, B. H., E. Pelinovsky, K. O. Kim, and J. S. Lee, 2003: Simulation of the trans-oceanic tsunami propagation due to the 1883 Krakatau volcanic eruption. *Nat. Hazards Earth Syst. Sci.*, **3**, 321–332, https://doi.org/10.5194/nhess-3-321-2003.

Chyba, C., P. Thomas, and K. Zahnle, 1993: The 1908 Tunguska explosion: Atmospheric disruption of a stony asteroid. *Nature*, **361**, 40–44, https://doi.org/10.1038/361040a0.

Cohn, S. E., and D. E. Dee, 1989: An analysis of the vertical structure equation for arbitrary thermal profiles. *Quart. J. Roy. Meteor. Soc.*, **115**, 143–171, https://doi.org/10.1002/qj.49711548508.

Cox, S. M., and P. C. Matthews, 2002: Exponential time differencing for stiff systems. *J. Comput. Phys.*, **176**, 430–455, https://doi.org/10.1006/jcph.2002.6995.

Denamiel, C., 2022: Destructive potential of planetary meteotsunami waves: ATAL ocean model results. Zenodo, https://doi.org/10.5281/zenodo.6503338.

——, J. Šepić, D. Ivanković, and I. Vilibić, 2019: The Adriatic Sea and Coast modelling suite: Evaluation of the meteotsunami forecast component. *Ocean Modell.*, **135**, 71–93, https://doi.org/10.1016/j.ocemod.2019.02.003.

——, X. Huan, J. Šepić, and I. Vilibić, 2020: Uncertainty propagation using polynomial chaos expansions for extreme sea level hazard assessment: The case of the eastern Adriatic meteotsunamis. *J. Phys. Oceanogr.*, **50**, 1005–1021, https://doi.org/10.1175/JPO-D-19-0147.1.

——, I. Tojčić, and I. Vilibić, 2022: Meteotsunamis in orography-free, flat bathymetry and warming climate conditions. *J. Geophys. Res. Oceans*, **127**, e2021JC017386, https://doi.org/10.1029/2021JC017386.

Dragoni, M., and D. Santoro, 2020: A model for the atmospheric shock wave produced by a strong volcanic explosion. *Geophys. J. Int.*, **222**, 735–742, https://doi.org/10.1093/gji/ggaa205.

Forbes, J. M., S. E. Palo, X. Zhang, Y. I. Portnyagin, N. A. Makarov, and E. G. Merzlyakov, 1999: Lamb waves in the lower thermosphere: Observational evidence and global consequences. *J. Geophys. Res.*, **104**, 17107–17115, https://doi.org/10.1029/1999JA900044.

Harrison, G., 2022: Pressure anomalies from the January 2022 Hunga Tonga–Hunga Ha'apai eruption. *Weather*, **77**, 87–90, https://doi.org/10.1002/wea.4170.

Holland, P. G., 1998: Manning formula. *Encyclopedia of Hydrology and Lakes*, Encyclopedia of Earth Science, Springer, https://doi.org/10.1007/1-4020-4497-6_149.

Kasahara, A., 1977: Numerical integration of the global barotropic primitive equations with Hough harmonic expansions. *J. Atmos. Sci.*, **34**, 687–701, https://doi.org/10.1175/1520-0469(1977)034<0687:NIOTGB>2.0.CO;2.

Kharif, C., and E. Pelinovsky, 2005: Asteroid impact tsunamis. *C. R. Phys.*, **6**, 361–366, https://doi.org/10.1016/j.crhy.2004.12.016.

Kring, D. A., H. J. Melosh, and D. M. Hunten, 1996: Impact-induced perturbations of atmospheric sulfur. *Earth Planet. Sci. Lett.*, **140**, 201–212, https://doi.org/10.1016/0012-821X(96)00050-7.

Lamb, H., 1911: On atmospheric oscillations. *Proc. Roy. Soc. London*, **A84**, 551–572, https://doi.org/10.1098/rspa.1911.0008.

Linares, A., C. H. Wu, A. J. Bechle, E. J. Anderson, and D. A. R. Kristovich, 2019: Unexpected rip currents induced by a meteotsunami. *Sci. Rep.*, **9**, 2105, https://doi.org/10.1038/s41598-019-38716-2.

Lowe, D. J., and W. P. de Lange, 2000: Volcano-meteorological tsunamis, thec. AD 200 Taupo eruption (New Zealand) and the possibility of a global tsunami. *Holocene*, **10**, 401–407, https://doi.org/10.1191/095968300670392643.

Luettich, R. A., R. H. Birkhahn, and J. J. Westerink, 1991: Application of ADCIRC-2DDI to Masonboro Inlet. A brief numerical modeling study. U.S. Army Engineer Waterways Experiment Station Rep., 27 pp., https://adcirc.org/wp-content/uploads/sites/2255/2018/11/1991_Luettich02.pdf.

Mason, B. G., D. M. Pyle, and C. Oppenheimer, 2004: The size and frequency of the largest explosive eruptions on Earth. *Bull. Volcanol.*, **66**, 735–748, https://doi.org/10.1007/s00445-004-0355-9.

Matoza, R. S., and Coauthors, 2022: Atmospheric waves and global seismoacoustic observations of the January 2022 Hunga eruption, Tonga. *Science*, **377**, 95–100, https://doi.org/10.1126/science.abo7063.

Morgan, J. V., T. J. Bralower, J. Brugger, and K. Wünnemann, 2022: The Chicxulub impact and its environmental consequences. *Nat. Rev. Earth Environ.*, **3**, 338–354, https://doi.org/10.1038/s43017-022-00283-y.

Ohno, S., and Coauthors, 2014: Production of sulphate-rich vapour during the Chicxulub impact and implications for ocean acidification. *Nat. Geosci.*, **7**, 279–282, https://doi.org/10.1038/ngeo2095.

Okal, E. A., and C. E. Synolakis, 2008: Far-field tsunami hazard from mega-thrust earthquakes in the Indian Ocean. *Geophys. J. Int.*, **172**, 995–1015, https://doi.org/10.1111/j.1365-246X.2007.03674.x.

——, and ——, 2016: Sequencing of tsunami waves: Why the first wave is not always the largest. *Geophys. J. Int.*, **204**, 719–735, https://doi.org/10.1093/gji/ggv457.

Pattiaratchi, C. B., and E. M. S. Wijeratne, 2015: Are meteotsunamis an underrated hazard? *Philos. Trans. Roy. Soc.*, **A373**, 20140377, https://doi.org/10.1098/rsta.2014.0377.

Pelinovsky, E., B. H. Choi, A. Stromkov, I. Didenkulova, and H.-S. Kim, 2005: Analysis of tide-gauge records of the 1883 Krakatau tsunami. *Tsunamis*, K. Satake, Ed., Advances in Natural and Technological Hazards Research, Vol. 23, Springer, 57–77, https://doi.org/10.1007/1-4020-3331-1_4.

Press, F., and D. Harkrider, 1962: Propagation of acoustic-gravity waves in the atmosphere. *J. Geophys. Res.*, **67**, 3889–3908, https://doi.org/10.1029/JZ067i010p03889.

——, and ——, 1966: Air-sea waves from the explosion of Krakatoa. *Science*, **154**, 1325–1327, https://doi.org/10.1126/science.154.3754.1325.

Pringle, W. J., 2020: Global storm tide modeling on unstructured meshes with ADCIRC, version 55—Simulation results and model setup. Zenodo, https://doi.org/10.5281/zenodo.3911282.

——, and K. Roberts, 2020: CHLNDDEV/OceanMesh2D: OceanMesh2D, version 3.0.0. Zenodo, https://doi.org/10.5281/zenodo.3721137.

——, D. Wirasaet, K. J. Roberts, and J. J. Westerink, 2021: Global storm tide modeling with ADCIRC v55: Unstructured mesh design and performance. *Geosci. Model Dev.*, **14**, 1125–1145, https://doi.org/10.5194/gmd-14-1125-2021.

Proudman, J., 1929: The effects on the sea of changes in atmospheric pressure. *Geophys. Suppl.*, **2**, 197–209, https://doi.org/10.1111/j.1365-246X.1929.tb05408.x.

Rabinovich, A. B., 2020: Twenty-seven years of progress in the science of meteorological tsunamis following the 1992 Daytona Beach event. *Pure Appl. Geophys.*, **177**, 1193–1230, https://doi.org/10.1007/s00024-019-02349-3.

Roberts, K. J., W. J. Pringle, and J. J. Westerink, 2019: OceanMesh2D 1.0: MATLAB-based software for two-dimensional unstructured mesh generation in coastal ocean modelling. *Geosci. Model Dev.*, **12**, 1847–1868, https://doi.org/10.5194/gmd-12-1847-2019.

Satake, K., M. Heidarzadeh, M. Quiroz, and R. Cienfuegos, 2020: History and features of trans-oceanic tsunamis and implications for paleo-tsunami studies. *Earth-Sci. Rev.*, **202**, 103112, https://doi.org/10.1016/j.earscirev.2020.103112.

Self, S., and M. R. Rampino, 1981: The 1883 eruption of Krakatau. *Nature*, **294**, 699–704, https://doi.org/10.1038/294699a0.

Taylor, G. I., 1929: Waves and tides in the atmosphere. *Proc. Roy. Soc. London*, **A126**, 169–183, https://doi.org/10.1098/rspa.1929.0213.

Themens, D., and Coauthors, 2022: Global propagation of ionospheric disturbances associated with the 2022 Tonga volcanic eruption. *Geophys. Res. Lett.*, **49**, e2022GL09815, https://doi.org/10.1029/2022GL098158.

Titov, V., A. B. Rabinovich, H. O. Mofjeld, R. E. Thomson, and F. I. González, 2005: The global reach of the 26 December 2004 Sumatra tsunami. *Science*, **309**, 2045–2048, https://doi.org/10.1126/science.1114576.

Vasylkevych, S., and N. Žagar, 2021: A high-accuracy global prognostic model for the simulation of Rossby and gravity wave dynamics. *Quart. J. Roy. Meteor. Soc.*, **147**, 1989–2007, https://doi.org/10.1002/qj.4006.

Vilibić, I., 2008: Numerical simulations of the Proudman resonance. *Cont. Shelf Res.*, **28**, 574–581, https://doi.org/10.1016/j.csr.2007.11.005.

VLIZ, 2022: Intergovernmental Oceanographic Commission (IOC) (2022): Sea level station monitoring facility. VLIZ, accessed 1 August 2022, https://doi.org/10.14284/482.

Weatherall, P., and Coauthors, 2021: GEBCO 2021 grid. British Oceanographic Data Centre, accessed 10 January 2023, https://doi.org/10.5285/c6612cbe-50b3-0cff-e053-6c86abc09f8f.

Wessel, P., and W. H. F. Smith, 1996: A global, self-consistent, hierarchical, high-resolution shoreline database. *J. Geophys. Res.*, **101**, 8741–8743, https://doi.org/10.1029/96JB00104.

Wright, C. J., and Coauthors, 2022: Surface-to-space atmospheric waves from Hunga Tonga-Hunga Ha'apai eruption. *Nature*, **609**, 741–746, https://doi.org/10.1038/s41586-022-05012-5.

Yeh, K. C., and C. H. Liu, 1974: Acoustic-gravity waves in the upper atmosphere. *Rev. Geophys.*, **12**, 193–216, https://doi.org/10.1029/RG012i002p00193.